HARDENING PROPERTIES OF GRANULATED BLAST FURNACE SLAG ACTIVATED BY FINE SLAG POWDERS FROM DIFFERENT SOURCES

Tomoyuki Hirano¹, *Hiroyuki Hara¹

¹Graduate School of Sciences and Technology for Innovation, Yamaguchi University, Japan

Received: 19 June 2025, Revised: 02 Sep. 2025, Accepted: 02 Oct. 2025

ABSTRACT: Granulated blast furnace slag (GBFS), when activated by an alkaline stimulant, GBFS releases chemical components and forms hydrates such as calcium silicate hydrate (C-S-H), leading to strength development and imparting cohesive properties despite its granular nature. However, because GBFS hardens slowly and its cohesive properties also varies, making it difficult to predict, this behavior is not reflected in Japanese design standards. To incorporate its cohesive properties into geotechnical design, a better understanding of its hardening behavior is required. Approaches to accelerate GBFS hardening is not only the addition of cement but also the addition of blast furnace slag powder (BFS-P) as an alkaline stimulant. However, the effectiveness of BFS-P varies depending on its production source. This study examined the hardening properties of GBFS mixed with three types of BFS-P sourced from different steel plants. Two moisture conditions—unsaturated and saturated—were considered to simulate applications in land and port structures. The results revealed that the MnO, Fe₂O₃, and TiO₂ contents in BFS-P significantly influenced GBFS hardening. A strong correlation was observed between compressive strength and hydrate content measured by thermogravimetric (TG) analysis at 30-600°C. Furthermore, the degree of saturation had a notable effect on strength development. Specifically, the hydrate content required for strength development was 0.283% and 0.376% in the unsaturated and saturated conditions. Unsaturated conditions, hydrates formed bridges between GBFS particles via the meniscus, which also increased the density of the hydrates themselves, resulting in higher strength despite lower levels of hydration reaction.

Keywords: Granulated Blast Furnace Slag, Blast Furnace Slag Powder, Unsaturated, Hydration

1. INTRODUCTION

Granulated Blast Furnace Slag (hereinafter referred to as GBFS) is an industrial by-product generated during pig iron production. It is produced by rapidly cooling the molten slag discharged from the blast furnace using a large volume of highpressure water, resulting in a predominantly amorphous structure. Due to its particle shape and size distribution, GBFS is classified as sandy soil and contains numerous air voids, which contribute to its high permeability and lightweight characteristics. Thanks to its amorphous nature, GBFS releases chemical components and forms hydrates-such as calcium silicate hydrate (C-S-H)—when activated by alkaline stimulant, leading to development. Consequently, despite being a granular material, GBFS exhibits high cohesiveness and is considered a promising geomaterial with excellent soil properties [1].

However, current Japanese utilization guidelines do not account for the cohesive behavior of GBFS [2], primarily because the hardening process is slow and the cause of the variation in cohesive properties depending on the GBFS used has not been clarified. This makes it difficult to predict the degree of cohesiveness that develops over time. To incorporate GBFS's cohesive properties into geotechnical design, a detailed understanding of its hardening behavior is

essential.

Blast furnace slag powder (hereinafter referred to as BFS-P) is used as a stabilizer to improve the engineering properties of soils [3–5]. Similarly, it can act as an alkaline stimulant for granular GBFS, and accelerate the hardening [6]. The increased specific surface area of BFS-P enhances the reaction rate. Nevertheless, few detailed studies have examined the hardening behavior of granular GBFS with different types of BFS-P. It has also been shown that differences in chemical composition occur when the production source of BFS-P differs [7,8]. In the field of concrete, numerous studies have shown that the chemical composition of BFS-P significantly affects hardening performance [8-12]. The influential components range from the major components of BFS-P such as CaO, SiO₂, Al₂O₃, and MgO to trace components such as TiO2, Fe2O3 and MnO. Furthermore, standards for blast furnace slag cement require BFS-P to meet a minimum basicity level.

These findings suggest that both the production source and the chemical composition of BFS-P strongly influence the strength development of GBFS when used as a geomaterial. However, these effects have rarely been investigated.

Therefore, this study aims to systematically investigate the hardening properties of GBFS with the addition of different BFS-P types obtained from various sources, under both saturated and unsaturated

conditions, to clarify the influence of BFS-P composition and moisture state on strength development.

2. RESEARCH SIGNIFICANCE

Most previous studies on the reactivity of BFS-P have focused on its application in combination with cement. However, the hydration reaction of GBFS is slower than that of cement, so it may be influenced by trace components contained in BFS-P and its reactivity as an alkaline stimulant for GBFS has not been investigated. In this study, three types of BFS-P produced by different steel plants were used to evaluate their effect on GBFS. Mechanical testing and instrumental analyses were conducted to assess the hardening behavior. The results demonstrate that the chemical properties of BFS-P significantly influence the hardening characteristics of GBFS, and these effects are discussed in detail.

3. EXPERIMENT SUMMARY

3.1 Materials

In this study, three types of BFS-P (hereinafter referred to as A, B, and C) were sourced from different steel plants. GBFS used in the experiments was sieved to pass through a 2 mm mesh. All BFS-P samples were free of gypsum and conformed to the JIS A 6206 standard. Table 1 presents the physical properties of the GBFS, while Table 2 summarizes the chemical composition and physical properties of each BFS-P. The primary components of BFS-P are CaO, SiO₂, and Al₂O₃. Basicity is used as one of the measures to evaluate the reactivity of BFS-P in blast furnace slag cement. In this study, basicity was also employed as an indicator of BFS-P reactivity and was calculated using Eq. (1).

$$b = \frac{\text{CaO} + \text{MgO} + \text{Al}_2 \text{O}_3}{\text{SiO}_2} \tag{1}$$

Among the three, BFS_B exhibited the highest basicity, followed by BFS_A and BFS_C. Fig. 1 displays the particle size distribution curves of the GBFS and the three BFS-P samples. All BFS-P types were significantly finer than the GBFS, and their particle size distributions were found to be similar.

3.2 Specimen Preparation Methods

In this study, cylindrical plastic molds with an inner diameter of 50 mm and a height of 100 mm were used to prepare the test specimens. The specimen preparation procedure is outlined as follows. Because the hardening properties of GBFS are influenced by the degree of saturation (S_r) , two moisture conditions—saturated and unsaturated—were

Table 1. Physical properties of GBFS

Soil particle density	$\rho_{\rm s}$ (Mg/m ³)	2.79
Maximum void ratio	$e_{ m max}$	1.273
Minimum void ratio	e_{min}	0.845

Table 2. Material properties of each BFS-P

Chemical composition (%)	A	A B	
CaO	48.1	46.8	47.1
SiO_2	31.1	30.1	30.6
Al_2O_3	12.9	14.2	12.0
MgO	4.75	4.75	4.90
SO_3	1.24	1.80	3.37
TiO_2	0.657	0.665	0.645
Fe_2O_3	0.336	0.438	0.409
MnO	0.168	0.335	0.324
K_2O	0.371	0.425	0.287
Na_2O	0.241	0.186	0.162
SrO	0.065	0.013	0.104
BaO	0.060	0.106	0.053
Soil particle density (Mg/m³)	2.89	2.90	2.91
Specific surface area (m ² /g)	0.396	0.460	0.429
Basicity b	2.114	2.184	2.092

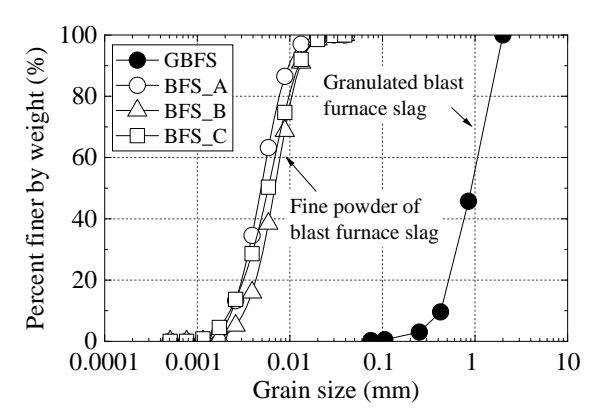


Fig. 1 Particle size of GBFS and BFS-P used in this study

simulated [13,14]. For the unsaturated condition, S_r was set to 30%, based on previous studies that reported high strength at this level.

Each of the three types of BFS-P was added as an alkaline stimulant to the GBFS specimens under both saturation conditions. GBFS hardening is accelerated by adding 8–10% BFS-P to its mass [6]. Thus, the addition rate of BFS-P was fixed at 10% of the GBFS mass. The relative density of the GBFS was set at 90%, calculated based on the maximum and minimum void ratios provided in Table 1. This corresponds to a combined dry density of GBFS and BFS-P of 1.623 Mg/m³. Using Eqs. (2) and (3), the required masses of GBFS and BFS-P to fill each mold were calculated accordingly.

$$m_{\rm sG} = \frac{\rho_{\rm sG} \times V \times 10^{-6}}{1 + \left\{ e_{\rm max} - \frac{D_{\rm r}}{100} (e_{\rm max} - e_{\rm min}) \right\}}$$
(2)

$$m_{\rm sB} = \frac{R_{\rm B}}{100} \times m_{\rm sG} \tag{3}$$

where m_{sG} is the mass of GBFS (g), m_{sB} is the mass of BFS-P (g), ρ_{sG} is the particle density of GBFS (Mg/m³), V is the volume of the specimen (m³), D_r is the relative density of GBFS (%), R_B is the addition rate of BFS-P (%), e_{max} and e_{min} are the maximum and minimum void ratios of GBFS, respectively.

Then, calculate the water content to adjust to each saturation level using the following equations:

$$w = \frac{\rho_{\rm w} \times e \times S_{\rm r}}{\rho_{\rm s}} \tag{4}$$

$$\rho_{\rm S} = \frac{100\rho_{\rm SG} + R_{\rm B} \times \rho_{\rm SB}}{100 + R_{\rm B}} \tag{5}$$

$$e = \frac{V - V_S}{V_C} \tag{6}$$

$$V_{\rm S} = \frac{m_{\rm SG}}{\rho_{\rm SG}} + \frac{m_{\rm SB}}{\rho_{\rm SB}} \tag{7}$$

where w is the water content (%), ρ_w is the density of water (Mg/m³), e is the void ratio, S_r is the degree of saturation (%), ρ_s is the density of the mixed sample of GBFS and BFS-P (Mg/m³), ρ_{sB} is the density of BFS-P (Mg/m³), and V_s is the volume of the mixed sample (m³).

For the unsaturated condition, ion-exchanged water was first added to the GBFS to achieve the specified water content. BFS-P was then added and thoroughly mixed to ensure uniform distribution. The prepared mixture was placed into the mold in 10 layers, with each layer compacted to reach the target density.

In contrast, the saturated specimens were prepared using the underwater drop method, as it was difficult to achieve full saturation using the compaction method described above. In this process, ion-exchanged water was poured into the mold in advance, and the GBFS-BFS-P mixture—adjusted to an appropriate water content—was divided into 10 portions and filled layer by layer into the mold using the underwater drop method.

3.3 Specimen Curing Methods

To prevent moisture loss due to evaporation during the curing period, the specimens were sealed using the following method. First, the top and bottom surfaces of each specimen were wrapped with plastic film. The entire specimen was then covered with aluminum foil and placed inside a light-shielding aluminum bag with a zipper closure. The bag was subsequently sealed at the top using a heat sealer to ensure airtight conditions. Fig. 2 shows the specimens

prepared with this moisture-prevention treatment.







(a) Wrapped in plastic warp

(b) Covered with aluminum foil

(c) Placed in aluminum bag with top welded

Fig. 2 Drying prevention treatment of specimen

All specimens were cured in a laboratory maintained at a constant temperature of 20 °C. The curing durations were set at 7, 28, 56, and 84 days. The experimental conditions are summarized in Table 3.

Table 3. Summary of experimental conditions

Name	Setting saturation	BFS-P	Curing time (days)
Unsaturated-A	Unsaturated	Α	7, 28, 56, 84
Saturated-A	Saturated	А	
Unsaturated-B	Unsaturated	В	
Saturated-B	Saturated	ь	
Unsaturated-C	Unsaturated	C	
Saturated-C	Saturated	C	

3.4 Experimental Procedure

3.4.1 Unconfined compression test

After the curing period, the specimens were demolded and subjected to unconfined compression testing. Three specimens were tested for each condition. For cases where the specimens were self-standing, the average value of the three test results was taken as the unconfined compressive strength. Specimens that could not maintain their shape and stand unsupported were excluded from mechanical testing.

The test procedure followed the JIS A 1216:2009 standard. To ensure uniform load application during testing, capping was applied to both the top and bottom surfaces of each specimen to smooth the loading interfaces. Dental gypsum was used as the capping material in this study.

3.4.2 Water content test and pH test

After the unconfined compression test, samples were collected from three locations: 0–10 mm, 45–55 mm, and 90–100 mm from the top of each specimen. Water content and pH tests were performed on these samples. The pH measurement followed the JGS 0211 standard (pH test of soil suspension) using a solid-to-liquid ratio of 1:5. A glass electrode-type pH meter was used for the measurements.

3.4.3 Thermogravimetric (TG) analysis

TG analysis was conducted on samples collected from a depth of 45–55 mm from the top of the specimen. As a pretreatment step, the samples were dried using a vacuum freeze-dryer. Minimal mass loss was observed after 48 hours, and therefore the freeze-drying duration was standardized to 48 hours. After drying, the samples were finely ground using a mortar and pestle prior to testing. The analysis was performed using the STA2500 Regulus (NETZSCH) under a nitrogen (N₂) flow rate of 50 mL/min. The heating rate was set to 20°C/min, and the temperature range spanned from 30 to 1000°C.

3.4.4 Ca elution test

The hydration reaction of GBFS with the addition of BFS-P is thought to proceed as calcium ions are eluted from BFS-P, contributing to the formation of an alkaline environment. To quantify the calcium elution, the following procedure was used:

- (1) Approximately 5 kg of BFS-P was air-dried, reduced via the cone and quartering method, and 300 g of the unaltered sample was obtained for analysis.
- (2) For the elution test, pure water was added to a polyethylene container (with stopcock), maintaining a sample-to-solvent weight ratio of 1:9. The mixture was agitated for 30 minutes using a shaker.
- (3) A portion of the slurry was filtered using a 0.45 μm membrane filter under suction; the resulting filtrate was used for calcium concentration measurements, while another portion was used for pH determination.
- (4) Calcium concentrations were determined using an ICP emission spectrometer, and the amount of calcium leached (C_{Ca}) was calculated accordingly.

4. EXPERIMENTAL RESULTS

4.1 Change in Degree of Saturation

Fig. 3 shows the change over time in the degree of saturation of the specimen. The degree of saturation was calculated using Eq. (8).

$$S_{\rm r} = \frac{w \times \rho_{\rm s}}{e \times \rho_{\rm w}} \tag{8}$$

There was no significant change in the degree of saturation during the curing period, regardless of the type of BFS-P used. In all experimental cases, the saturation level at 7 days of curing was lower than the initially set value. As the specimens were sealed in aluminum bags, it is unlikely that drying effects contributed to this change. Therefore, it is considered that some of the pore water was consumed in hydration reactions during the hardening of GBFS,

and the resulting hydrates did not evaporate during oven drying. Furthermore, even under saturated conditions, the degree of saturation remained significantly lower than the target value.

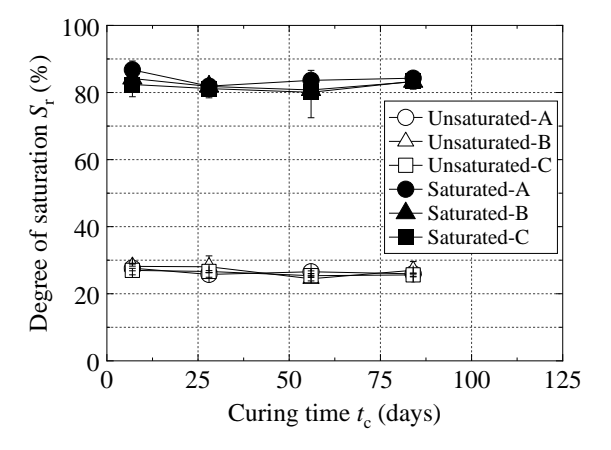


Fig. 3 Change in degree of saturation over time

Fig. 4 shows the depth profile of saturation using BFS_A as an example. The top surface of the specimen was defined as a depth of 0 mm. The deeper areas have slightly higher saturation, suggesting that some of the pore water has flowed down.

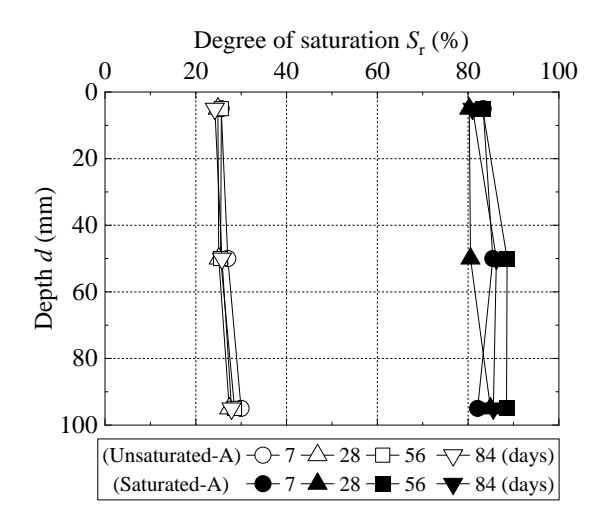


Fig. 4 Depth distribution of degree of saturation for conditions using BFS_A

4.2 Change in Unconfined Compressive Strength

Fig. 5 shows the evolution of unconfined compressive strength over time. Strength increased with curing duration across all conditions. Notably, unsaturated conditions exhibited higher strength than saturated ones, regardless of BFS-P type. At 7 days, only specimens containing BFS_A developed measurable strength. By 56 days, Unsaturated-C outperformed Unsaturated-A, and by 84 days, Unsaturated-B exceeded Unsaturated-A.

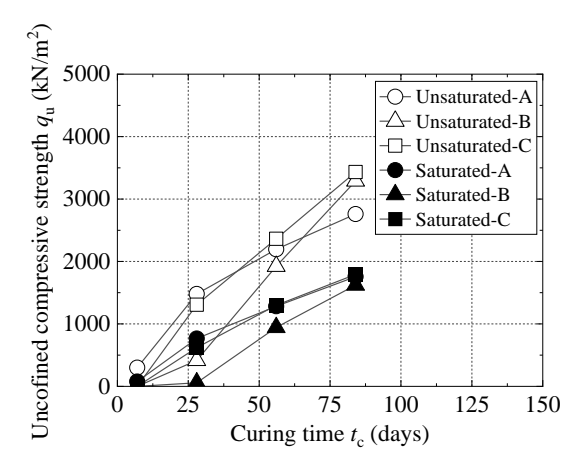


Fig. 5 Change in unconfined compressive strength $q_{\rm u}$ over time

4.3 Evaluation of the Curing Behavior of GBFS with Different BFS-P

The hardening behavior of GBFS was evaluated in this study. As reported previously, the compressive strength of GBFS increases in proportion to the square root of curing time [15]. Fig. 6 shows the relationship between unconfined compressive strength q_u and the square root of curing time t_c . The dashed lines in the figure represent approximation lines fitted using Eq. (9).

$$q_{\rm u} = \alpha \sqrt{t_{\rm c} - t_0} \tag{9}$$

where α is the hardening rate coefficient, t_c is the curing time (days), and t_0 is time required to start hardening (days). The results confirmed that the unconfined compressive strength of GBFS generally increases in proportion to the square root of curing time, regardless of the degree of saturation; all cases exhibited high coefficients of determination.

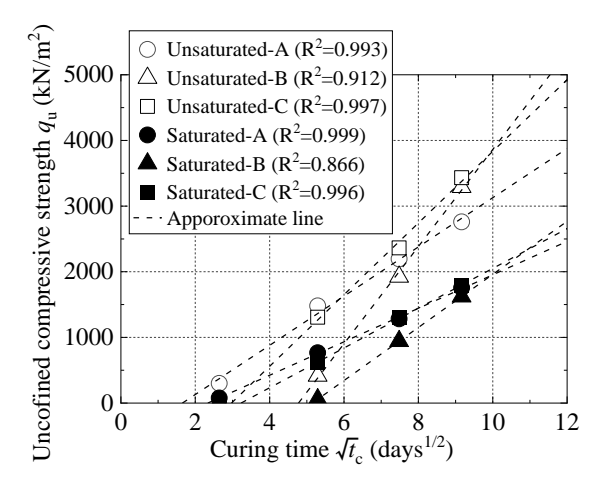


Fig. 6 Unconfined compressive strength $q_{\rm u}$ and square root of curing time $t_{\rm c}$

However, both the slope of the approximated line and the time required to start hardening varied depending on the BFS-P type and the saturation. Accordingly, the hardening rate coefficient (α) and the time required to start hardening (t_0) were extracted for each experimental condition.

Fig. 7 shows the α and t_0 values for all conditions. For the same BFS-P, the unsaturated condition yielded a higher α and a smaller t_0 compared to the saturated condition. Among the three BFS-P types, BFS_B exhibited the highest values of both α and t_0 under both saturation states. This indicates that, under the same saturation level, a longer induction period before hardening is associated with a more rapid subsequent strength gain.

This behavior is attributed to the kinetics of the initial hydration reaction. Fig. 8 shows a conceptual diagram of the difference in hydrate formation depending on the hydration rate. When hydration proceeds too rapidly, the resulting hydrates may not sufficiently infiltrate the interparticle spaces, leading to a higher void ratio and lower strength. In contrast, slower hydration allows the hydrates to diffuse and precipitate more uniformly throughout the GBFS matrix, thereby reducing the void ratio and significantly enhancing strength development [16].

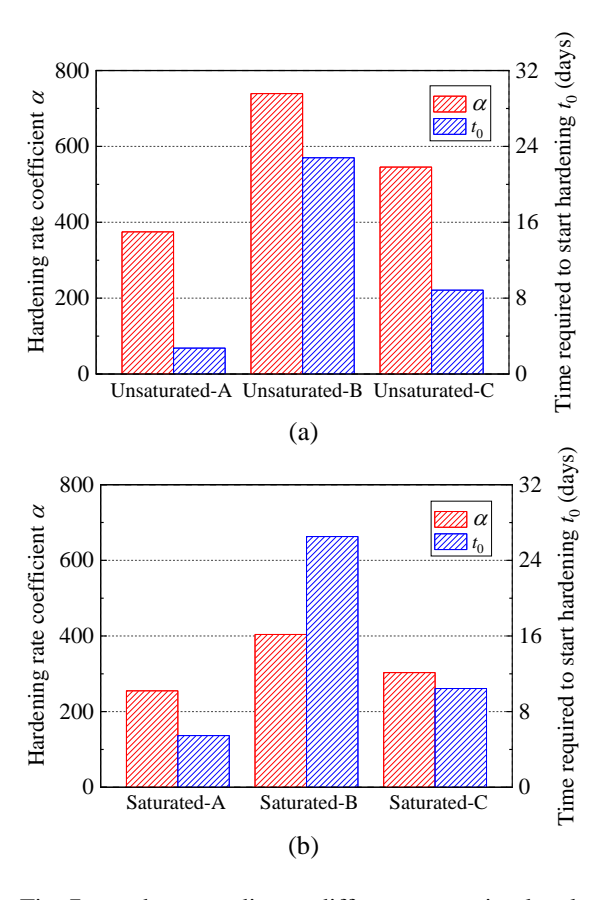


Fig. 7 α and t_0 according to different saturation levels and BFS-P types: (a) Unsaturated condition, (b) Saturated condition

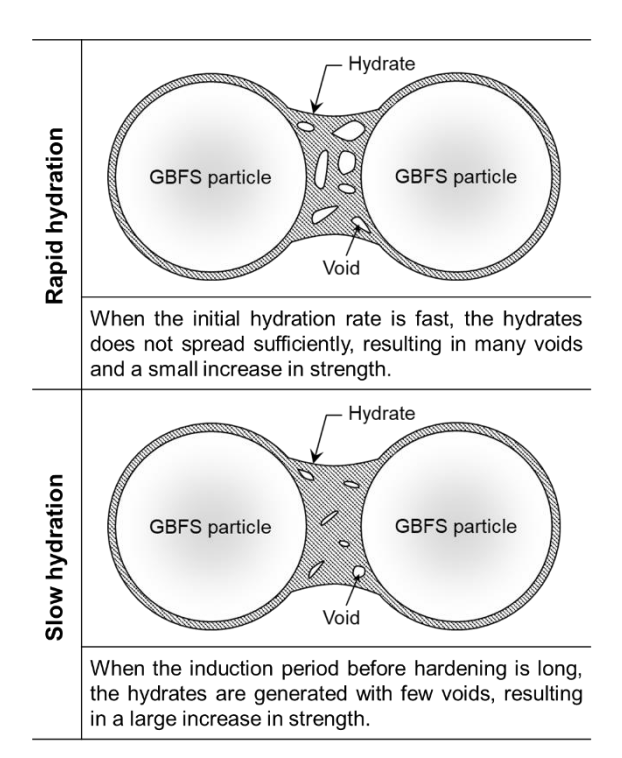


Fig. 8 Conceptual diagram of the difference in hydrate formation depending on the hydration rate

In this study, BFS_C exhibited the highest compressive strength at the end of the 84-day curing period. However, it is presumed that BFS_B would eventually achieve the highest strength with extended curing time.

Fig. 9 shows the relationship between basicity and the initial hardening time t_0 , revealing an inverse correlation—higher basicity is associated with a longer delay before hardening commences. This finding suggests that basicity alone may not be a suitable indicator of BFS-P reactivity when used as an alkaline stimulant for GBFS, highlighting the need for a more comprehensive reactivity index.

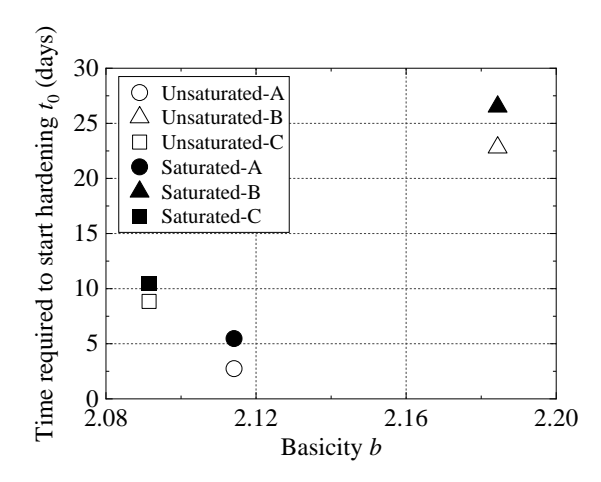


Fig. 9 Relationship between basicity and t_0

Previous studies have reported that certain trace oxide components, specifically MnO, Fe₂O₃, and TiO₂, can inhibit the initial hydration reaction of slag [8,17–19]. Given that these chemical species exert different levels of influence on the hardening process, applying weighting factors may be required to evaluate their individual effects more precisely [18,19]. However, due to limitations in quantifying these individual contributions in the present study, the total concentration of MnO, Fe₂O₃, and TiO₂ was collectively defined as the Hydration Inhibition Index (H_i) , as expressed in Eq. (10).

$$H_{\rm i} = m_{\rm MnO} + m_{\rm Fe_2O_3} + m_{\rm TiO_2} \tag{10}$$

Fig. 10 shows the relationship between H_i and t_0 . The t_0 tends to increase with increasing H_i . Fig. 11 shows the relationship between H_i and C_{Ca} . The C_{Ca} was clearly lower for larger H_i . Therefore, when the BFS-P contains a larger amount of MnO, Fe₂O₃, and TiO₂, calcium elution is delayed, requiring a longer time to transition into an alkaline environment, and hardening takes a longer.

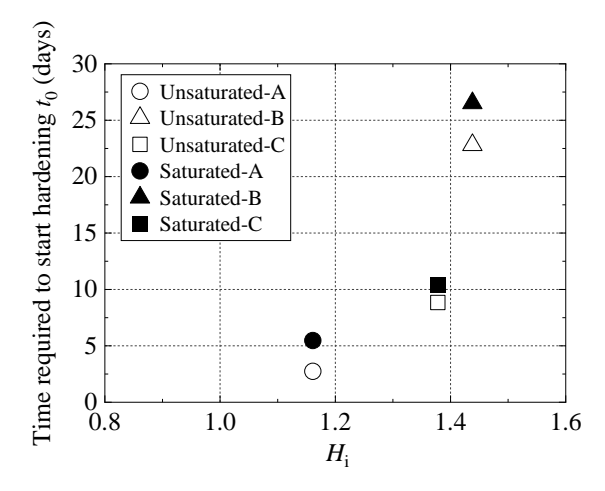


Fig. 10 Relationship between H_i and t_0

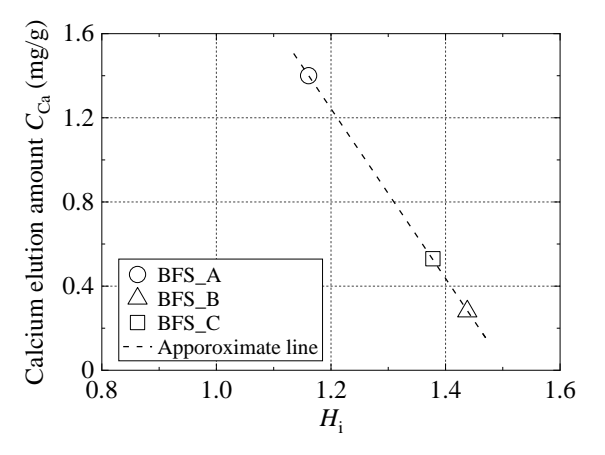


Fig. 11 Relationship between H_i and C_{Ca}

This suggests that trace amounts of oxides in BFS-P influence the hardening properties of GBFS, and indicates the limitation of evaluating its hardening properties solely on the basis of basicity.

4.4 Change in pH

Fig. 12 shows the change in pH over time. The saturated condition tended to exhibit a higher pH than the unsaturated condition. After 56 days of curing, the pH value remained almost constant, showing approximately 12.0 and 11.8 in the saturated and unsaturated conditions, respectively. This suggests that the pH of GBFS does not continue to increase indefinitely with curing time but eventually converges. The convergence of pH is considered to result from the ion concentrations of calcium, silica, and others in the pore water reaching a steady state, after which the amount of calcium consumed by hydration reactions balances with the amount of calcium released.

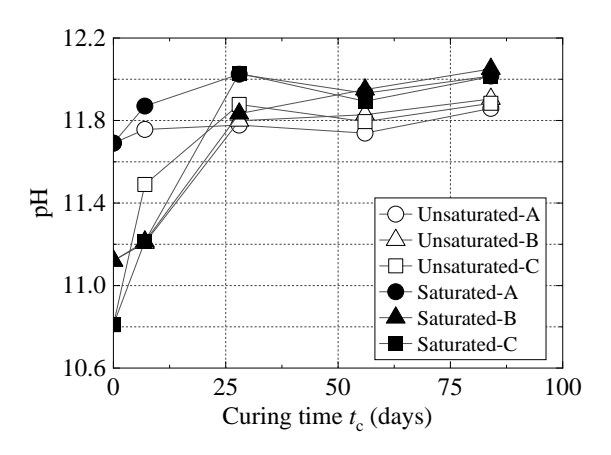


Fig. 12 Change in pH over time

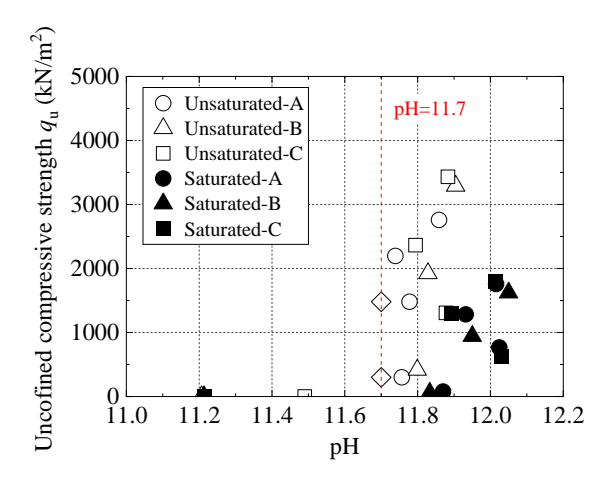


Fig. 13 Relationship between pH and unconfined compressive strength $q_{\rm u}$

Fig. 13 shows the relationship between pH and unconfined compressive strength. It was confirmed

that when the pH exceeds 11.7, the material becomes self-standing and begins to harden. After hardening, the pH remained around 11.7 to 12.1, regardless of the magnitude of unconfined compressive strength. Although the saturated condition exhibited higher pH, the compressive strength was higher in the unsaturated condition, indicating that pH and compressive strength do not necessarily correlate.

4.5 TG Analysis

In thermogravimetric (TG) analysis, changes such as decomposition and combustion caused by heating are measured as weight loss. For GBFS, the total weight loss up to 600° C is considered a relative indicator of the degree of hydration [16]. Therefore, the rate of mass loss from 30 to 600° C, denoted as ΔH , was used as an index of hydration progress. Fig. 14 shows the change in ΔH over time for each condition. Under all conditions, ΔH generally increased with curing time. BFS_A exhibited a higher ΔH in the saturated condition compared to the unsaturated condition after 7 days of curing. A similar trend was observed for BFS_B and BFS_C after 56 days and 28 days, respectively. These results broadly correspond to the timing of strength development.

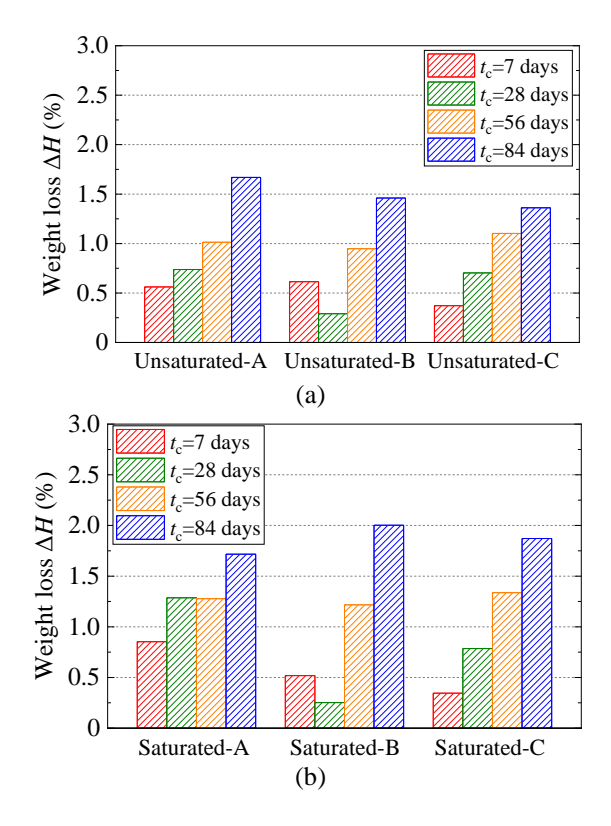


Fig. 14 Change in weight loss ΔH over time according to different saturation levels and BFS-P types : (a) Unsaturated condition, (b) Saturated condition

Fig. 15 shows the relationship between ΔH and unconfined compressive strength $q_{\rm u}$ under

unsaturated and saturated conditions. It was confirmed that hydration progressed and strength increased for both saturation levels. The coefficient of determination (R^2) of the approximated line was 0.846 and 0.890 for the unsaturated and saturated conditions, respectively. Under unsaturated states, the formation of hydrates bridging between GBFS particles via menisci, as well as increased densification of the hydrates themselves. In contrast, under saturated states, hydrates are formed uniformly throughout the voids, and more hydrates are formed than under unsaturated states, but the density is lower [13]. The slope of each approximated line and the ΔH value at which strength begins to occur depend on the moisture state. The slope of approximated line was 2618.9 for the unsaturated condition and 1142.0 for the saturated condition. The ΔH value at which $q_{\rm u}$ equals zero on the approximated line was 0.283% for the unsaturated condition and 0.376% for the saturated condition. This suggests that under unsaturated conditions, strength develops with relatively little hydrate formation and the large rate of strength increase. As shown in Fig. 13, despite the high pH under saturated conditions, the low strength is likely due to the formation of low-density hydrates.

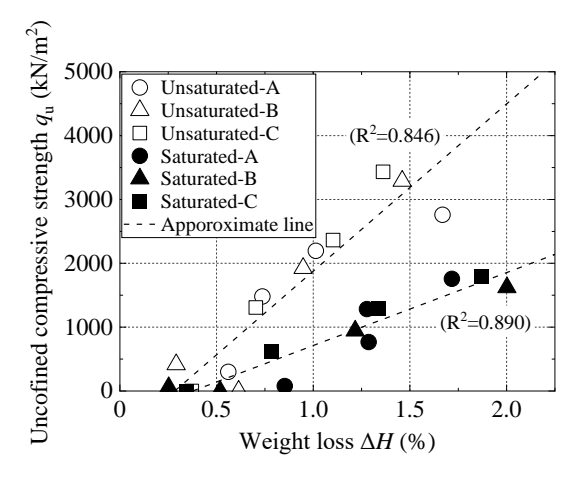


Fig. 15 Relationship between ΔH and unconfined compressive strength $q_{\rm u}$

5. CONCLUSIONS

This study examined the hardening properties of different BFS-P types when added to GBFS as alkaline stimulant. The main findings are as follows:

- (1) The hardening properties of GBFS vary depending on the chemical composition of the BFS-P used as an alkaline stimulant.
- (2) In the same saturation level, the longer delay before strength development generally corresponds to a greater subsequent increase in strength. When the same BFS-P is used, unsaturated state takes less time to harden and has higher strength.
- (3) The amounts of MnO, Fe₂O₃, and TiO₂ in BFS-P

- strongly influence the hardening behavior of GBFS.
- (4) Regardless of BFS-P type, pH converges to approximately 11.7–12.1 after hardening, and there is no direct correlation between pH and compressive strength.
- (5) There is a strong correlation between hydration amount and compressive strength. The ΔH value at which $q_{\rm u}$ equals zero on the approximated line was 0.283% for the unsaturated condition and 0.376% for the saturated condition. Compared to saturated conditions, the unsaturated state achieves higher strength with less hydrate formation, likely due to hydrates bridging between GBFS particles via menisci and increased densification of the hydrates.

This study revealed that trace amounts of oxides contained in BFS-P affect the hardening properties of GBFS. In the future, with the accumulation of data, it may become possible to predict the strength development of GBFS from the composition of the BFS-P to be added. This is important for incorporating the cohesive properties of GBFS into geotechnical design.

6. ACKNOWLEDGMENTS

This study was conducted with support from the Nippon Slag Association, Japan and the Japan Society for the Promotion of Science (JSPS KAKENHI Grant Number 22K04314).

7. REFERENCES

- [1] Nippon Slag Association, Blast Furnace Granulated Slag, Technical Data as Civil Engineering Materials, 2009, pp. 1-86.
- [2] Ministry of Land, Infrastructure, Transport and Tourism, Recycling Guidelines for Port and Airport Maintenance, 2024, pp. 184-222.
- [3] Nuruddin M., Moghal A. A. B., Rasheed R. M., Sravya G. G. K., Balaramakrishna R., Vyshnavi Y., Coupled Effect of Ground Granulated Blast Slag and Bagasse Fibers to Enhance the Compressive Strength and Durability Characteristics of Expansive Soil, Geotechnical Frontiers 2025, 2025, pp.323-331.
- [4] Banaian M., Fattahi S. M., Soroush A., Komaei A., Triaxial Behavior and Microstructural Insights of Loose Sandy Soil Stabilized with Alkali Activated Slag, Scientific Reports, Vol. 15, No. 1, 2025, 3573.
- [5] Shakil M., Nazar S., Ameen H. F. M., Shahzad A., Ahmad F., A Comparative Study of Ground Granulated Blast Furnace Slag and Bagasse Ash Incorporation on Enhancing Mechanical Properties of Expansive Soil, Results in Engineering, Vol. 25, 2025, 103569.
- [6] Kikuchi Y., Nakashima K., Kimura J., Mizutani

- T., Solidification Acceleration and Solidified Shear Strength Evaluation of Granulated Blast Furnace Slag, J. JSCE C (Geotech. Eng.), Vol. 67, No. 1, 2011, pp. 145-159.
- [7] Hasumi T., Ikeo Y., Influence of Mix Proportion of Cement and Curing Temperature on Strength Development of Blast Furnace Slag-Gypsum Cement Using Recycled Concrete Powder, Cement Science and Concrete Technology, Vol. 70, No. 1, 2016, pp. 557-563.
- [8] Bougara A., Lynsdale C., Milestone N.B., Reactivity and Performance of Blastfurnace Slags of Differing Origin, Cement & Concrete Composites, Vol. 32, No. 4, 2010, pp. 319-324.
- [9] Ben Haha M., Lothenbach B., Le Saout G., Winnefeld F., Influence of Slag Chemistry on the Hydration of Alkali-Activated Blast-Furnace Slag - Part I: Effect of MgO. Cement and Concrete Research, Vol. 41, No. 9, 2011, pp. 955–963.
- [10] Ainie M. D. A., Jamaluddin N., Azlina A. H. N., Siok H. C., A Review: GGBS as a Cement Replacement in Concrete, Earth and Environmental Science, Vol. 1022, No. 1, 2022, 012044.
- [11] Nito N., Ueda Y., Matsuzawa K., Sakai E., Influences of Chemical Compositions and Fineness of Blast Furnace Slag on Strength and Hydration of High Volume Blast Furnace Slag Cement, Cement Science and Concrete Technology, Vol.74, No.1, 2020, pp.15-21.
- [12] Ahmad J., Kontoleon K. J., Majdi A., Naqash M. T., Deifalla A. F., ben Kahla N., Isleem H. F., Qaidi S. M. A., A Comprehensive Review on the Ground Granulated Blast Furnace Slag (GGBS) in Concrete Production, Sustainability, Vol. 14, No. 14, 2022, 8783.

- [13] Hara H., Nasu E., Hardening Characteristics of Granulated Blast Furnace Slag with Different Degrees of Saturation, Construction and Building Materials, Vol. 424, 2024, 135942.
- [14] Hara H., Hardening Characteristics of Granulated Blast Furnace Slag Under Saturated and Unsaturated Conditions, Japanese Geotechnical Journal, Vol. 17, No. 3, 2022, pp. 277-284.
- [15] Wada M., Matsuda H., Hara H., Nakamura S., Igawa N., Quantitative Evaluation of Strength and Self-Restorative Capacity of Granulated Blast Furnace Slag, Journal of the Society of Materials Science, Japan, Vol. 65, No. 1, 2016, pp. 28-33.
- [16] Ben Haha M., Le Saout G., Winnefeld F., Lothenbach B., Influence of Activator Type on Hydration Kinetics, Hydrate Assemblage and Microstructural Development of Alkali Activated Blast-Furnace Slags, Cement and Concreate Research, Vol. 41, No. 3, 2011, pp. 301-310.
- [17] Xing J., Zhao Y., Qiu J., Sun X., Microstructural and Mechanical Properties of Alkali Activated Materials from Two Types of Blast Furnace Slags, Materials, Vol. 12, No. 13, 2019, 2089.
- [18] Tobo H., Okuyama H., Arima K., Yuge M., Okada M., Oono A., Influence of MnO on Activity of Ground Granulated Blast Furnace Slag, JFE-technical report, No. 40, 2017, pp. 75-79.
- [19] Ito T., Misumi H., Takahashi T., Influences of Chemical Components on the Activity Index of CaO-Al2O3-SiO2-MgO-System Slag, Cement Science and Concrete Technology, Vol. 70, No. 1, 2016, pp. 222-229.

Copyright $^{\odot}$ Int. J. of GEOMATE All rights reserved, including making copies, unless permission is obtained from the copyright proprietors.